

## A 2-terminal perovskite/silicon multijunction solar cell enabled by a silicon tunnel junction

Jonathan P. Mailoa,<sup>1,a),b)</sup> Colin D. Bailie,<sup>2,a)</sup> Eric C. Johlin,<sup>1</sup> Eric T. Hoke,<sup>2</sup> Austin J. Akey,<sup>1</sup> William H. Nguyen,<sup>2</sup> Michael D. McGehee,<sup>2,b)</sup> and Tonio Buonassisi<sup>1,b)</sup>

<sup>1</sup>Massachusetts Institute of Technology, Cambridge, Massachusetts 02139, USA

<sup>2</sup>Stanford University, Stanford, California 94305, USA

(Received 4 February 2015; accepted 23 February 2015; published online 24 March 2015)

With the advent of efficient high-bandgap metal-halide perovskite photovoltaics, an opportunity exists to make perovskite/silicon tandem solar cells. We fabricate a monolithic tandem by developing a silicon-based interband tunnel junction that facilitates majority-carrier charge recombination between the perovskite and silicon sub-cells. We demonstrate a  $1\text{ cm}^2$  2-terminal monolithic perovskite/silicon multijunction solar cell with a  $V_{OC}$  as high as 1.65 V. We achieve a stable 13.7% power conversion efficiency with the perovskite as the current-limiting sub-cell, and identify key challenges for this device architecture to reach efficiencies over 25%. © 2015 AIP Publishing LLC. [<http://dx.doi.org/10.1063/1.4914179>]

Solar-to-electricity conversion efficiency is the technical variable that most strongly influences silicon (Si) photovoltaic (PV) module costs.<sup>1,2</sup> The record efficiency of crystalline silicon (c-Si) single-junction PV devices has increased from 25% to 25.6% during the last fifteen years,<sup>3,4</sup> asymptotically approaching the 29.4% Auger-recombination-constrained Shockley-Queisser limit.<sup>5</sup> To make PV modules with higher efficiency than market-leading c-Si while leveraging existing c-Si manufacturing capacity, Si-based tandem approaches have been proposed.<sup>6–10</sup> The top sub-cell in a silicon-based tandem should have a band gap between 1.6 and 1.9 eV.<sup>11</sup> However, very few materials exhibit high open-circuit voltages ( $V_{OC}$ ) within this band gap range. Recently, the methylammonium-lead-halide perovskite has demonstrated a rapid efficiency increase<sup>12–16</sup> with a  $V_{OC}$  of 1.15 V.<sup>17</sup> The methylammonium-lead-halide perovskite has a tunable band gap, ranging from 1.6 to 2.3 eV depending on halide composition,<sup>18</sup> though not all compositions are currently stable under illumination.<sup>19</sup> Methods to optically transmit longer-wavelength light through a top perovskite sub-cell in a mechanically stacked tandem configuration have been developed recently.<sup>9,20</sup>

A perovskite/Si multijunction solar cell may also be constructed *via* monolithic integration where a thin film perovskite sub-cell is deposited directly onto the c-Si sub-cell. Monolithic integration requires electrical coupling between sub-cells and transmission of infrared light to the bottom sub-cell. We use an interband tunnel junction<sup>21</sup> to facilitate electron tunneling from the electron-selective contact of the perovskite sub-cell into the *p*-type emitter of the Si sub-cell. This approach stands in contrast to the recombination layer used in other perovskite tandem systems<sup>22</sup> and is the one widely used in III-V<sup>23</sup> and micromorph (*a*-Si/ $\mu$ c-Si)<sup>24</sup> tandem solar cells. Unlike the tunnel junction in III-V multijunction solar cells, our tunnel junction is made of silicon with an indirect band gap, enabling electrical coupling

with minimal parasitic absorption. The conduction-band alignment between Si and the perovskite sub-cell's electron-selective contact ( $\text{TiO}_2$ ) enables bypassing the usage of a transparent conducting oxide (TCO) recombination layer, an alternative option with greater parasitic absorption. In this work, we use the methylammonium-lead(II)-iodide perovskite ( $\text{CH}_3\text{NH}_3\text{PbI}_3$ ), which has a 1.61 eV band gap.<sup>25</sup> Herein, we present the device design, fabrication, characterization, and loss analysis of monolithic perovskite/Si multijunction solar cells.

We develop a 2-terminal perovskite/Si multijunction architecture on an *n*-type Si solar cell (Figure 1(a)) with  $1\text{ cm}^2$

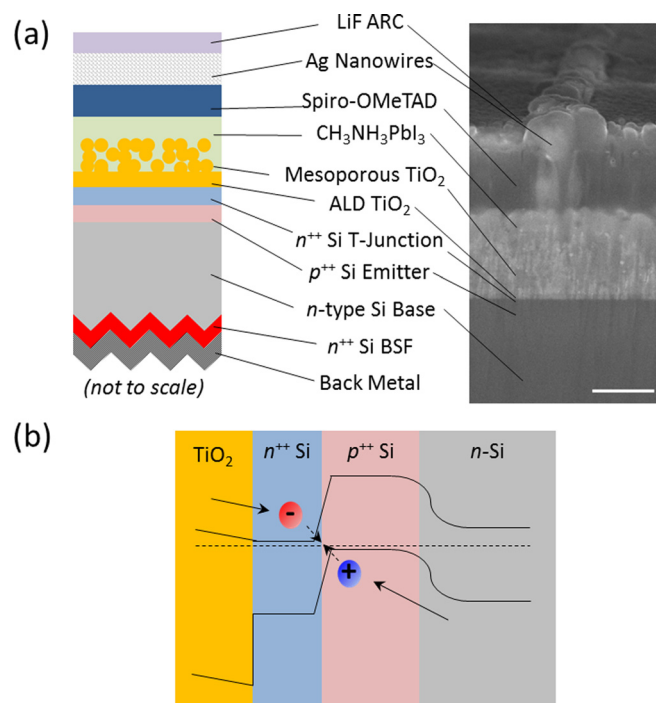


FIG. 1. (a) The device structure of a 2-terminal monolithically grown perovskite/Si multijunction solar cell with an *n*-type Si base. The polished SEM image is taken at  $45^\circ$  tilt to show the Ag nanowire mesh (500 nm scale bar). (b) Band diagram of the perovskite/silicon cell interface showing the charge-transport mechanism around the Si tunnel junction.

<sup>a)</sup>J. P. Mailoa and C. D. Bailie contributed equally to this work

<sup>b)</sup>Authors to whom correspondence should be addressed. Electronic addresses: jpmailoa@alum.mit.edu; mmcgehee@stanford.edu; and buonassisi@mit.edu

area. We process an  $n$ -type Si sub-cell with planar top surface and full-area  $p$ -type emitter and  $n$ -type back surface field (BSF) using standard Si processing techniques.<sup>26</sup> A tunnel junction facilitates carrier recombination (holes from the  $n$ -type Si base passing through the  $p$ -type emitter and electrons from the perovskite layer passing through its TiO<sub>2</sub> electron transport layer, respectively, as shown in Figure 1(b)). We form an  $n^{++}/p^{++}$  tunnel junction by depositing heavily doped  $n^{++}$  hydrogenated amorphous silicon (a-Si:H) using plasma-enhanced chemical vapor deposition (PECVD).<sup>26</sup> The 30 nm-thick a-Si:H layer is subsequently annealed in N<sub>2</sub> ambient at 680 °C for 15 min to activate the dopants.<sup>27</sup> It is known that interdiffusion of dopant species during the device fabrication process (such as the dopant activation anneal) may degrade the tunnel junction conductivity. Accordingly, a 2–3 nm-thick intrinsic a-Si layer is inserted between the  $p^{++}$  emitter and the  $n^{++}$  amorphous Si layer during the PECVD process<sup>26</sup> to mitigate possible dopant interdiffusion.<sup>28</sup> After the dopant-activation anneal, the amorphous layers are partially crystallized as shown by transmission electron microscopy (TEM, Figure 2(a)). Using secondary ion mass spectrometry (SIMS), we show the dopant concentration on the  $n^{++}/p^{++}$  Si interface after the dopant activation anneal is  $10^{19}$ – $10^{20}$  cm<sup>-3</sup>, which is suitable to form a high-quality inter-band tunnel junction (Figure 2(b)).<sup>28</sup>

The addition of the tunnel junction on top of the single-junction  $n$ -type solar cell slightly reduces the short-circuit current ( $J_{SC}$ ), but the presence of the tunnel junction has a

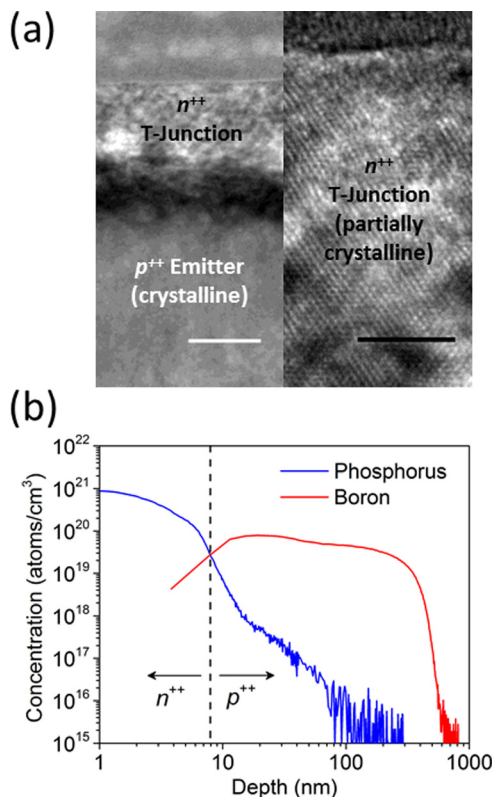


FIG. 2. (a) TEM image of the  $n^{++}/p^{++}$  silicon tunnel junction interface after the dopant activation annealing (left: 30 nm scale bar) and high-resolution TEM image of the  $n^{++}$  layer, showing the partially crystalline nature of this layer (right: 5 nm scale bar). (b) SIMS profile of the Si emitter and tunnel junction layer showing the sharp doping profile at the tunnel junction interface.

negligible effect on the series resistance (Figure S1) indicating proper operation of the tunnel junction.<sup>26</sup> The slight reduction in  $J_{SC}$  is due to parasitic absorption at  $\lambda < 500$  nm (Figure S2),<sup>26</sup> which does not affect tandem performance as this portion of the spectrum is absorbed in the perovskite cell before reaching the tunnel junction.

The efficiency of the planar single-junction Si cells is 13.8%. This efficiency is lower than commercial averages in part due to tandem design considerations. These intentional design considerations are: (1) No surface texturing for light trapping is applied because a planar front surface simplifies deposition of the perovskite; (2) No  $p$ -type front surface passivation scheme is applied on the emitter because the same technique cannot be implemented on the  $n$ -type portion of the tunnel junction. Other causes of lower efficiency are: (1) full-area BSF passivation only provides moderate passivation; (2) a front surface passivation scheme that can be decoupled from the tunnel junction formation needs to be developed; (3) dedicated clean furnaces for emitter formation and back surface passivation are necessary to make more efficient Si sub-cells.

We fabricate the monolithic perovskite/Si multijunction solar cell by depositing a perovskite sub-cell on top of the tunnel junction. We first metallize the back of our Si sub-cell, then deposit a 30 nm-thick TiO<sub>2</sub> layer on the planar  $n^{++}$  c-Si front surface using atomic layer deposition (ALD).<sup>26</sup> This TiO<sub>2</sub> layer is the  $n$ -type heterojunction for the perovskite sub-cell. It is known that TiO<sub>2</sub> is a good electron-selective contact for c-Si because of its conduction-band alignment,<sup>29</sup> which also eases electron transport from the TiO<sub>2</sub> layer into the  $n^{++}$  Si tunnel junction layer.<sup>30,31</sup> The thickness of this ALD TiO<sub>2</sub> layer can impact the optical transmission into the Si sub-cell (Figure S3),<sup>26</sup> and hence further thickness optimization is needed. The perovskite is deposited onto a mesoporous TiO<sub>2</sub> layer in a two-step conversion method.<sup>15,26</sup> An organic  $p$ -type heterojunction contact, spiro-OMeTAD, is deposited by spin-coating on top of the perovskite and is chemically doped with spiro-(TSFI)<sub>2</sub>.<sup>32</sup> The top silver nanowire (AgNW) electrode is deposited using the procedure developed by Bailie *et al.*<sup>9</sup> AgNWs are sprayed from solution onto a plastic (PET) film, and then transferred from the PET to the spiro-OMeTAD layer via mechanical transfer through the application of pressure via a ball bearing. The silver nanowire electrode before transfer has a sheet resistance of 9  $\Omega/\square$  with a peak transmission of 89.5%. A 111-nm-thick lithium fluoride (LiF) anti-reflection layer is then deposited by thermal evaporation.

The  $J$ - $V$  curve of our 2-terminal perovskite/Si multijunction solar cell under simulated AM1.5G illumination is shown in Figure 3(a). Due to the hysteresis often observed in metal-halide perovskite solar cells, it is important to be rigorous with  $J$ - $V$  characterization.<sup>33</sup> We use a 5 s delay after each 100 mV voltage step before measuring the current in both scan directions. However, we still find hysteresis at this scan rate and that up to 30 s is required to reach a steady-state. This yields an overestimation of the efficiency when scanning from forward to reverse bias and an underestimation when scanning from reverse to forward bias.<sup>33</sup> We measure the steady-state values of the three critical points on the  $J$ - $V$  curve: open circuit ( $V_{OC}$ ), short circuit ( $J_{SC}$ ), and the

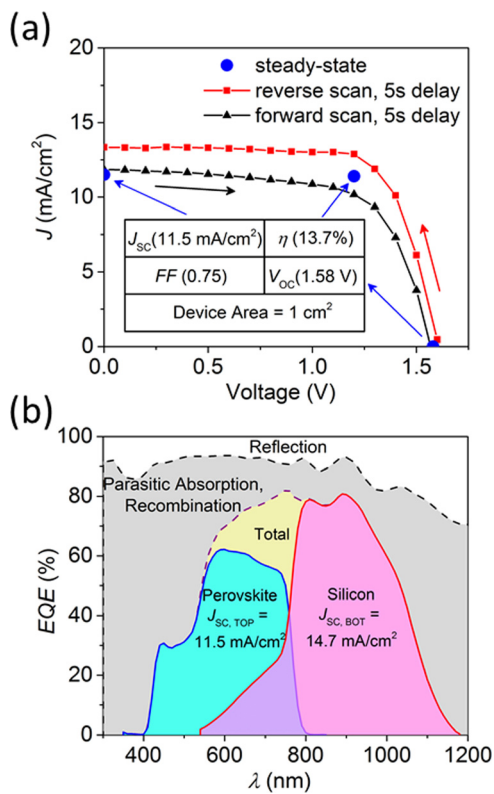


FIG. 3. (a)  $J$ - $V$  curve of the 2-terminal perovskite/silicon multijunction solar cell under AM1.5G illumination. Forward and reverse-bias scan directions are shown with 5 s measurement delay per data point. Steady-state values for  $J_{SC}$ ,  $V_{OC}$ , and MPP are measured by averaging over 30 s after reaching steady state. (b) Total device reflection and EQE of the perovskite and Si sub-cells of a typical perovskite/Si multijunction cell. The perovskite sub-cell EQE is corrected to match the measured  $J_{SC}$  and the silicon sub-cell EQE is reported as measured.<sup>26</sup>

maximum power point (MPP), depicted as blue circles (color online) in Figure 3(a) to negate hysteretic effects. The steady-state  $J_{SC}$  is 11.5 mA/cm<sup>2</sup>, the steady-state  $V_{OC}$  is 1.58 V, and the steady-state MPP is 13.7% at 1.20 V bias (Figure S4).<sup>26</sup> These resultant fill factor ( $FF$ ) is 0.75. The 1 cm<sup>2</sup> cell was aperture-masked to ensure a correct illumination area. The  $V_{OC}$  has been measured as high as 1.65 V in some devices. This result is encouraging, as the  $V_{OC}$  is approximately the sum of the  $V_{OC}$  for the perovskite top sub-cell and the bottom Si sub-cell illuminated through a separate semi-transparent perovskite device on FTO<sup>9</sup> (approximately 1.05 V and 0.55 V, respectively), further indicating proper operation of the tunnel junction.

The slow current-dynamics and corresponding hysteresis observed in the tandem resemble the sluggish dynamics of our perovskite solar cells and suggest that the perovskite sub-cell limits the current of the tandem.<sup>33</sup> This finding is substantiated by external quantum efficiency (EQE) measurements (Figure 3(b)) of the individual sub-cells.<sup>26</sup> Our tandem  $J_{SC}$  of 11.5 mA/cm<sup>2</sup> is low because the perovskite is illuminated through the  $p$ -type heterojunction, opposite from conventional perovskite devices. To understand the directional dependence of illumination on the perovskite sub-cell, we illuminate a semi-transparent single-junction perovskite solar cell<sup>9</sup> through the TiO<sub>2</sub> heterojunction and through the spiro-OMeTAD heterojunction. When illuminated through

the TiO<sub>2</sub> heterojunction, the EQE of the semi-transparent cell integrates to 17.3 mA/cm<sup>2</sup>, whereas when illuminated through the spiro-OMeTAD heterojunction the EQE integrates to 11.4 mA/cm<sup>2</sup> (Figure S5) due to low EQE for  $\lambda < 550$  nm.<sup>26</sup> We attribute the lower photocurrent from the spiro-OMeTAD-side to parasitic absorption by the doped spiro-OMeTAD layer. From absorption measurements of doped spiro-OMeTAD on glass (Figure S6),<sup>26</sup> we estimate that the absorbed flux of the AM1.5G spectrum in this layer is 6.4 mA/cm<sup>2</sup> from 300–750 nm. We find that parasitic absorption by spiro-OMeTAD also reduces the photocurrent available to the bottom Si sub-cell, absorbing the equivalent of 2.0 mA/cm<sup>2</sup> of infrared photons from 750–1200 nm. The parasitic absorption can be reduced with a thinner spiro-OMeTAD layer, which is currently optimized to planarize a rough perovskite top surface to enable deposition of the silver nanowire electrode. With smoother perovskite films, the spiro-OMeTAD layer can achieve planarization with a thinner layer. The parasitic absorption may be completely removed by replacement of spiro-OMeTAD with an alternate  $p$ -type heterojunction contact that simultaneously exhibits both good conductivity and low parasitic absorption.

The perovskite sub-cell is also limited by quality of the perovskite absorber. Our single-junction perovskite cells with gold back contacts fabricated as control devices achieve at best 13.5% efficiency. Optimization of deposition conditions, precursor materials, and annealing protocols along with replacement or reduction of the spiro-OMeTAD layer is expected to yield a perovskite top sub-cell equivalent to the record single-junction perovskite cell, which currently stands at 20.1%.<sup>3</sup> For the Si sub-cell, applying a back-surface field and excellent surface passivation to the back of the bottom Si sub-cell, using dedicated furnaces, and decoupling the front surface passivation scheme from the tunnel junction formation are expected to yield improvements. We predict a Si sub-cell with a  $V_{OC}$  of 660–720 mV and a matched tandem  $J_{SC}$  of 18–19 mA/cm<sup>2</sup> when illuminated through the perovskite sub-cell. We expect, with these changes designed to improve the sub-cells to the match the highest quality devices available today, the monolithic tandem would have a  $V_{OC}$  of 1.84 V, a  $J_{SC}$  of 19 mA/cm<sup>2</sup>, a  $FF$  of 0.83, and a corresponding efficiency of 29.0%. Ultimately, it has been suggested that perovskite/Si monolithic tandems can surpass 35% efficiency through careful photon management.<sup>10</sup>

In summary, we have demonstrated a 1 cm<sup>2</sup>, 2-terminal monolithically-integrated metal-halide perovskite/Si multijunction solar cell. The monolithic integration is enabled by a Si-based tunnel junction fabricated directly on top of the bottom Si sub-cell emitter and by incorporating a semi-transparent silver nanowire-based top electrode. We obtained a multijunction device  $V_{OC}$  as high as 1.65 V, which is the expected sum of the perovskite and filtered Si  $V_{OC}$ 's, demonstrating the potential of this approach. The best 2-terminal multijunction prototype device efficiency is 13.7% and is current-limited by the perovskite sub-cell. This value is low compared to the record efficiency for perovskite or Si cells, in part because this tandem prototype does not yet have best-in-class perovskite and Si layers. Further improvements can be achieved by replacing the spiro-OMeTAD layer with wider band gap hole transport material, improving the

quality of the perovskite absorber, use of dedicated furnaces for the Si sub-cell fabrication, and by implementing better surface passivation schemes on the front and back side of the Si sub-cell. These improvements can yield a 29.0% efficient tandem, with the ultimate efficiency potential of these monolithic tandems surpassing 35%.

H. Wagner, J. Z. Lee, S. C. Siah, and S. E. Sofia (MIT) are thanked for silicon cell design advice. Y. S. Lee (MIT), A. Scheuermann (Stanford), and M. Hathaway (Harvard CNS) are thanked for ALD TiO<sub>2</sub> deposition advice. Z. K. Ren, N. S. Khanghah, I. M. Peters (SMART), H. Liu, Z. Liu, L. Fen (SERIS), R. Jones-Albertus (DOE) and S. A. Ringel (Ohio State University) are thanked for helpful discussions. This work was supported by Bay Area Photovoltaic Consortium (BAPVC) under Contract No. DE-EE0004946, and the U.S. Department of Energy (DOE) under Contract No. DE-EE0006707. This work was performed in part at the Center for Nanoscale Systems (CNS), a member of the National Nanotechnology Infrastructure Network (NNIN), which is supported by the National Science Foundation under NSF award no. ECS-0335765.

<sup>1</sup>P. A. Basore, *IEEE J. Photovoltaics* **4**, 1477 (2014).

<sup>2</sup>D. M. Powell, M. T. Winkler, A. Goodrich, and T. Buonassisi, *IEEE J. Photovoltaics* **3**, 662 (2013).

<sup>3</sup>M. A. Green, K. Emery, Y. Hishikawa, W. Warta, and E. D. Dunlop, *Prog. Photovoltaics Res. Appl.* **23**, 1 (2015).

<sup>4</sup>K. Masuko, M. Shigematsu, T. Hashiguchi, D. Fujishima, M. Kai, N. Yoshimura, T. Yamaguchi, Y. Ichihashi, T. Mishima, N. Matsubara, T. Yamanishi, T. Takahama, M. Taguchi, E. Maruyama, and S. Okamoto, *IEEE J. Photovoltaics* **4**, 1433 (2014).

<sup>5</sup>R. M. Swanson, in Proceedings of 31st IEEE Photovoltaic Specialist Conference (2005), Vol. 889.

<sup>6</sup>M. Umeno, T. Soga, K. Baskar, and T. Jimbo, *Sol. Energy Mater. Sol. Cells* **50**, 203 (1998).

<sup>7</sup>K. Tanabe, K. Watanabe, and Y. Arakawa, *Sci. Rep.* **2**, 349 (2012).

<sup>8</sup>Z. M. Beiley and M. D. McGehee, *Energy Environ. Sci.* **5**, 9173 (2012).

<sup>9</sup>C. D. Bailie, M. G. Christoforo, J. P. Mailoa, A. R. Bowring, E. L. Unger, W. H. Nguyen, J. Burschka, N. Pellet, J. Z. Lee, M. Grätzel, R. Noufi, T. Buonassisi, A. Salleo, and M. D. McGehee, *Energy Environ. Sci.* **8**, 956 (2015).

<sup>10</sup>P. Loper, B. Niesen, S.-J. Moon, S. Martin de Nicolas, J. Holovsky, Z. Remes, M. Ledinsky, F.-J. Haug, J.-H. Yum, S. De Wolf, and C. Ballif, *IEEE J. Photovoltaics* **4**, 1545 (2014).

<sup>11</sup>F. Meillaud, A. Shah, C. Droz, E. Vallat-Sauvain, and C. Miazza, *Sol. Energy Mater. Sol. Cells* **90**, 2952 (2006).

<sup>12</sup>M. Liu, M. B. Johnston, and H. J. Snaith, *Nature* **501**, 395 (2013).

<sup>13</sup>M. M. Lee, J. Teuscher, T. Miyasaka, T. N. Murakami, and H. J. Snaith, *Science* **338**, 643 (2012).

<sup>14</sup>J.-H. Im, C.-R. Lee, J.-W. Lee, S.-W. Park, and N.-G. Park, *Nanoscale* **3**, 4088 (2011).

<sup>15</sup>J. Burschka, N. Pellet, S.-J. Moon, R. Humphry-Baker, P. Gao, M. K. Nazeeruddin, and M. Grätzel, *Nature* **499**, 316 (2013).

<sup>16</sup>N. J. Jeon, J. H. Noh, W. S. Yang, Y. C. Kim, S. Ryu, J. Seo, and S. Il Seok, *Nature* **517**, 476 (2015).

<sup>17</sup>A. Ishii, A. K. Jena, and T. Miyasaka, *APL Mater.* **2**, 091102 (2014).

<sup>18</sup>J. H. Noh, S. H. Im, J. H. Heo, T. N. Mandal, and S. Il Seok, *Nano Lett.* **13**, 1764 (2013).

<sup>19</sup>E. T. Hoke, D. J. Slotcavage, E. R. Dohner, A. R. Bowring, H. I. Karunadasa, and M. D. McGehee, *Chem. Sci.* **6**, 613 (2015).

<sup>20</sup>P. Löper, S.-J. Moon, S. Martin de Nicolas, B. Niesen, M. Ledinsky, S. Nicolay, J. Bailat, J.-H. Yum, S. De Wolf, and C. Ballif, *Phys. Chem. Chem. Phys.* **17**, 1619 (2015).

<sup>21</sup>L. Esaki, *Phys. Rev.* **109**, 603 (1958).

<sup>22</sup>T. Todorov, T. Gershon, O. Gunawan, C. Sturdevant, and S. Guha, *Appl. Phys. Lett.* **105**, 173902 (2014).

<sup>23</sup>G. J. Bauhuis, P. Mulder, and J. J. Schermer, *Prog. Photovoltaics Res. Appl.* **22**, 656 (2014).

<sup>24</sup>F. A. Rubinelli, J. K. Rath, and R. E. I. Schropp, *J. Appl. Phys.* **89**, 4010 (2001).

<sup>25</sup>K. Tvingstedt, O. Malinkiewicz, A. Baumann, C. Deibel, H. J. Snaith, V. Dyakonov, and H. J. Bolink, *Sci. Rep.* **4**, 6071 (2014).

<sup>26</sup>See Supplementary Material at <http://dx.doi.org/10.1063/1.4914179> for fabrication and characterization details.

<sup>27</sup>Y. Wang, X. Liao, Z. Ma, G. Yue, H. Diao, J. He, G. Kong, Y. Zhao, Z. Li, and F. Yun, *Appl. Surf. Sci.* **135**, 205 (1998).

<sup>28</sup>N. Jin, S. Chung, A. T. Rice, P. R. Berger, P. E. Thompson, C. Rivas, R. Lake, S. Sudirgo, J. J. Kempisty, B. Curanovic, S. L. Rommel, K. D. Hirschman, S. K. Kurinec, P. H. Chi, and D. S. Simons, *IEEE Trans. Electron Devices* **50**, 1876 (2003).

<sup>29</sup>D. Gebeyehu, C. J. Brabec, N. S. Sariciftci, D. Vangeneugden, and R. Kiebooms, *Synth. Met.* **125**, 279 (2001).

<sup>30</sup>S. Avasthi, W. E. McClain, G. Man, A. Kahn, J. Schwartz, and J. C. Sturm, *Appl. Phys. Lett.* **102**, 203901 (2013).

<sup>31</sup>J. Jhaveri, S. Avasthi, K. Nagamatsu, and J. C. Sturm, in Proceedings of 40th IEEE Photovoltaic Specialist Conference (2014), Vol. 1525.

<sup>32</sup>W. H. Nguyen, C. D. Bailie, E. L. Unger, and M. D. McGehee, *J. Am. Chem. Soc.* **136**, 10996 (2014).

<sup>33</sup>E. L. Unger, E. T. Hoke, C. D. Bailie, W. H. Nguyen, A. R. Bowring, T. Heumüller, M. G. Christoforo, and M. D. McGehee, *Energy Environ. Sci.* **7**, 3690 (2014).

## Supplementary Online Material

### A 2-Terminal Perovskite/Silicon Multijunction Solar Cell Enabled by a Silicon Tunnel Junction

Jonathan P. Mailoa<sup>1†\*</sup>, Colin D. Bailie<sup>2†</sup>, Eric C. Johlin<sup>1</sup>, Eric T. Hoke<sup>2</sup>, Austin J. Akey<sup>1</sup>, William H. Nguyen<sup>2</sup>, Michael D. McGehee<sup>2</sup>, Tonio Buonassisi<sup>1\*</sup>

<sup>1</sup>Massachusetts Institute of technology, Cambridge, MA 02139, USA

<sup>2</sup>Stanford University, Stanford, CA 94305, USA

\*Corresponding author: [jpmailoa@alum.mit.edu](mailto:jpmailoa@alum.mit.edu), [mmcgehee@stanford.edu](mailto:mmcgehee@stanford.edu), [buonassisi@mit.edu](mailto:buonassisi@mit.edu)

†These authors contributed equally to this work

### Silicon Sub-Cell Fabrication Procedure

We first start with a double-side polished <100> *n*-type float zone silicon (Si) wafer (1–5 Ω-cm, 300 μm thickness). The front side of the wafer is then coated with a 300 nm-thick silicon nitride (SiN<sub>x</sub>) film, which protects the planarity of the Si front surface during the subsequent random pyramidal texturing step (3% weight KOH solution in DI mixed with isopropanol (6:1 volume), 80°C etch for 20 minutes) on the back side of the wafer. After removing the SiN<sub>x</sub> protective layer using hydrofluoric acid (HF), we clean the sample using RCA cleaning procedure (RCA1 = 10 minute, 80°C dip in 5:1:1 NH<sub>4</sub>OH:H<sub>2</sub>O<sub>2</sub>:H<sub>2</sub>O, RCA2 = 10 minute, 80°C dip in 5:1:1 HCl:H<sub>2</sub>O<sub>2</sub>:H<sub>2</sub>O): deionized (DI) water dip → HF dip → RCA1 clean → DI water dip → HF dip → DI water dip → RCA2 clean → DI water dip → HF dip → DI water dip → N<sub>2</sub> drying. We then implant boron on the planar front surface (<sup>11</sup>B with 1.8×10<sup>15</sup> cm<sup>-2</sup> dose, 6 keV implantation energy) and phosphorus on the textured back surface (<sup>31</sup>P with 4×10<sup>15</sup> cm<sup>-2</sup> dose, 10 keV implantation energy) of the wafer. After cleaning the wafer again using RCA cleaning procedure, we dip the wafer in dilute HF solution for oxide removal, clean it with DI water and dry it with N<sub>2</sub>. Then we

simultaneously form the  $p$ -type B emitter and  $n$ -type P back surface field (BSF) by drive-in annealing at 960°C in an  $N_2$  ambient for 30 minutes.

After the emitter and BSF formation, we clean the wafers again with RCA cleaning procedure, and then perform dilute HF oxide removal, DI water dip, and  $N_2$  drying. We then form and create our  $n^{++}/p^{++}$  tunnel junction interface by depositing heavily doped  $n^{++}$  hydrogenated amorphous silicon (a-Si:H) using plasma-enhanced chemical vapor deposition (PECVD). We first deposit a 2–3 nm-thick intrinsic a-Si layer on top of the  $p^{++}$  emitter using the PECVD process (temperature of 250°C, pressure of 150 mTorr, 55 sccm of  $SiH_4$  gas with a plasma power density of 0.16 W/cm<sup>2</sup>). Afterwards, a 30 nm-thick a-Si:H layer is deposited at 250°C at a pressure of 200 mTorr (55 sccm of  $SiH_4$  gas and 50 sccm of 1%  $PH_3$  in  $H_2$  gas) and plasma power density of 0.13 W/cm<sup>2</sup>. Subsequently, the Si sample is annealed in  $N_2$  ambient at 680°C for 15 minutes to activate the dopants and partially crystallize the amorphous layer.

After the tunnel junction formation, we form 1.1×1.1 cm<sup>2</sup> square-shaped mesa spaced 1.4×1.4 cm<sup>2</sup> apart. This is done using photolithography. We deposit positive photoresist on both sides of the wafer (Shipley 1813 photoresist spun at 4000 rpm for 40 s, baked at 115°C for 1 minute). The front side undergoes mesa patterning and is exposed for 4.5 s, and developed in CD-26 developer for approximately 1 minute), while the back side is left unexposed to protect the BSF on the back side during the subsequent mesa formation step. The mesa formation is then done on the front side of the Si wafer using reactive ion etching (RIE) to etch 300 nm of the Si layer (removing the entire  $n^{++}$  tunnel junction and most of the  $p^{++}$  emitter) outside the square-shaped mesa to reduce the dark current. The remaining photoresist mask is then removed using solvent clean (3 minute sonication in acetone, 3 minute sonication in IPA, rinsing with DI water and drying with  $N_2$ ).

We perform dilute HF oxide removal, DI water dip, and  $N_2$  drying. We then form the back (negative) metal contact by electron-beam evaporation. A layer stack of Ti/Pd/Ag/Pt with layer

thicknesses of 20/20/300/30 nm is chosen (Ti for adhesion, Pd for metal diffusion barrier, Ag for electrical conduction, and Pt for corrosion protection during perovskite sub-cell processing) followed by rapid thermal anneal (400°C in N<sub>2</sub> for 5 minutes) to improve metal adhesion.

We again perform dilute HF oxide removal, DI water dip, and N<sub>2</sub> drying before depositing 30 nm-thick TiO<sub>2</sub> layer on the planar c-Si device using atomic layer deposition of a tetrakis(dimethylamido)titanium (TDMAT) precursor (Cambridge NanoTech Savannah ALD tool, 150°C substrate temperature, 80°C precursor temperature, 440 mTorr base pressure, and 20 sccm N<sub>2</sub> carrier gas). To achieve the desired TiO<sub>2</sub> thickness, we apply 604 cycles of pulsing H<sub>2</sub>O vapor for 0.02 s, waiting for 7 s, pulsing TDMAT vapor for 0.2 s, and waiting for 7 s. It is worth noting that the thickness of this ALD TiO<sub>2</sub> layer can impact on the optical transmission into the bottom Si sub-cell (**Figure S3**), and hence further thickness optimization is needed. After the TiO<sub>2</sub> ALD deposition, we deposit photoresist on the top for TiO<sub>2</sub> protection (Shipley 1818 photoresist spun at 4000 rpm for 40 s, baked at 115°C for 1 minute). Dilute HF with 10% concentration in DI is then used to dissolve the TiO<sub>2</sub> layer which got deposited on the back metal during the ALD process. Finally, the tunnel junction substrates are then laser-scribed from the back to form 1.4×1.4 cm<sup>2</sup> substrates. After mechanical cleaving, we have 1.4×1.4 cm<sup>2</sup> tunnel junction substrates with 1.1×1.1 cm<sup>2</sup> square-shaped mesa (active junction area) in the middle and TiO<sub>2</sub> layer on the planar front surface protected by photoresist.

## Tunnel Junction Functionality Analysis

We further confirm the functionality of the Si-based interband tunnel junction by fabricating single-junction *n*-type Si solar cells out of the tunnel-junction substrates. We apply an 80 nm-thick SiN<sub>x</sub> anti-reflection coating (ARC) on the planar front surface of the Si cell, as well as front finger and back metallization using a Ti/Pd/Ag stack. We show in **Figure S1** that the addition of the tunnel junction on top of the single-junction *n*-type solar cell slightly reduces the short-circuit current ( $J_{sc}$ ), but the interband tunnel junction has a negligible effect on the series resistance. The measured series resistances ( $R_s$ ) of a cell with and without a tunnel junction are 1.03  $\Omega\text{-cm}^2$  and 1.08  $\Omega\text{-cm}^2$ , respectively. The  $R_s$  of the cell without a tunnel junction is larger than the cell with a tunnel junction because the  $R_s$  addition from the tunnel junction itself is smaller than the sample-to-sample  $R_{SE}$  variability of our c-Si cell fabrication process.

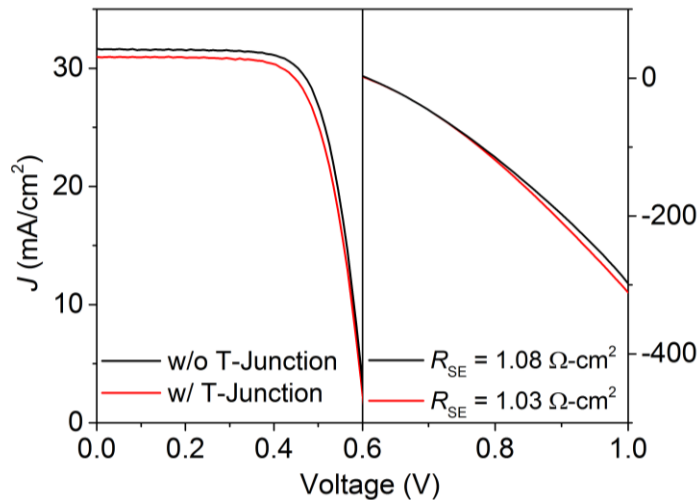


**Figure S1.** Comparison of  $J$ - $V$  profile for identical Si cells with and without a tunnel junction, showing negligible effect of the tunnel junction to the single-junction Si cell performance.

While the thin layer of Si composing the interband tunnel junction on the top of our cell degrades the blue response (300–400 nm light) of our device and reduces  $J_{sc}$  from 31.6 mA/cm<sup>2</sup> to 31.0 mA/cm<sup>2</sup>, in practice this effect is negligible, as only perovskite-filtered light with wavelength  $\lambda > 500$  nm is incident on the bottom Si sub-cell in the tandem. The external quantum efficiency (EQE) of our Si sub-cells (**Figure S2**) confirms the negligible parasitic absorption of the tunnel junction for  $\lambda > 500$  nm. It is worth noting that our interband tunnel junction has low parasitic absorption because it is made from partially crystallized Si, which is an indirect band gap material. This is in contrast with III-V-based interband tunnel junctions where the tunnel junction layer thicknesses need to be minimized to reduce the parasitic absorption.

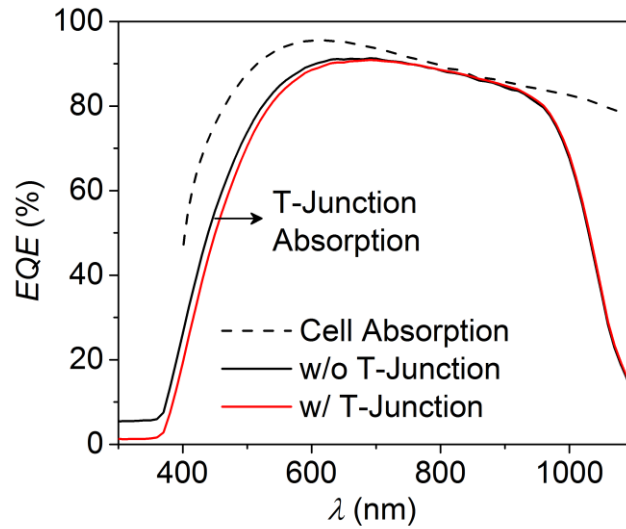


**Figure S2.** EQE curve of single-junction *n*-type silicon cells with and without a tunnel junction. This curve shows negligible parasitic absorption in the tunnel junction for wavelength  $\lambda > 500$  nm.

## Effect of TiO<sub>2</sub> Compact Layer Thickness on Transmission into Silicon Sub-Cell

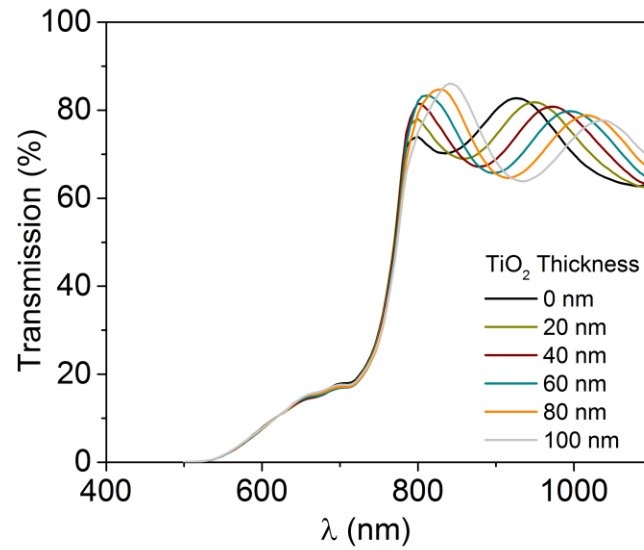


**Figure S3.** Light transmission into the bottom Si sub-cell in a 2-terminal perovskite/silicon multijunction configuration for different planar ALD TiO<sub>2</sub> thicknesses simulated using finite-difference-time-domain (FDTD) simulation.

## Perovskite Sub-Cell Fabrication Procedure

The tunnel junction substrates were then shipped with a protective photoresist layer. The substrates were prepared for further processing by sonication in acetone for 5 minutes, sonication in IPA for 5 minutes, rinsing with DI water and drying with  $N_2$ , 5 minutes of UV-ozone cleaning, and sintering for 30 minutes at 450°C. After cooling down, mesoporous  $TiO_2$  films were spun onto the  $TiO_2$  surface at 4000 rpm for 30 s and sintered at 450°C. The spin-coating solution was a 1:3 dilution of 18-NRT  $TiO_2$  paste (Dyesol) in ethanol.

All previous steps were performed in ambient atmosphere. The remainder of device fabrication was performed in a  $N_2$  glovebox with <5 ppm  $O_2$  and  $H_2O$ . The  $TiO_2$  substrates were dried by heating to 500°C with a hot air gun for 30 minutes and immediately brought into the glovebox. A 1.3 M  $PbI_2$  solution was prepared by dissolving  $PbI_2$  (Aldrich, 211168) into anhydrous DMF (Acros, 32687) and stirring on a hotplate at 100°C. The DMF was filtered through a 200 nm PTFE filter (Pall, 4552) prior to adding to the solution in order to remove particulates. Methylammonium iodide (MAI) was purchased from Dyesol and used as received. A solution of 10 mg MAI per 1 mL anhydrous IPA (Acros, 61043) was prepared and allowed to dissolve at room temperature. A pure IPA rinse solution was prepared as well. The IPA was filtered through a 20 nm PTFE filter prior to adding to the solutions in order to remove particulates.

After the  $TiO_2$  substrates were cooled to room temperature, 100  $\mu L$  of the 100°C  $PbI_2$ /DMF solution was pipetted onto the substrate and spun at 6500 rpm for 90 s. The resulting film was dried for 30 minutes on a 70°C hotplate. After cooling, the films were dipped in the MAI/IPA solution for 15 minutes. Films were then rinsed in IPA, dried by spinning at 4000 rpm for 30 s, and placed back on the 70°C hotplate for 30 minutes. After cooling, 75  $\mu L$  of a spiro-OMeTAD (Lumtec, LT-S922) solution was

spun on top at 4000 rpm for 30 s. The spiro-OMeTAD solution was 163 mM spiro-OMeTAD in anhydrous chlorobenzene (Sigma-Aldrich, 284513). The spiro-OMeTAD was dissolved by placing on a hotplate at 70°C for more than 30 minutes. 534 mM of tert-butyl pyridine (Aldrich, 142379) and 86 mM of Li-TFSI (Aldrich, 15224) dissolved as 520 mg/mL in anhydrous acetonitrile (Acros, 61096) were added to the spiro-OMeTAD solution. In this study, 8 mol% of the spiro-OMeTAD was spiro-OMeTAD(TFSI)<sub>2</sub>, resulting in 16% of spiro-OMeTAD molecules being chemically oxidized to ensure conductivity in the spiro-OMeTAD layer. The spiro-OMeTAD(TFSI)<sub>2</sub> was synthesized as reported elsewhere in literature. After the spiro-OMeTAD solution was prepared, it was filtered through a 20 nm Al<sub>2</sub>O<sub>3</sub> filter (Whatman, 6809-3102) to remove any aggregates and particulates. Films were then removed from the glovebox and stored overnight in a desiccator at 20% RH.

An AgNW film on PET was transferred on top of the spiro-OMeTAD film similar to previously reported procedures.<sup>1</sup> A change was made to use a spring-loaded ball bearing to better control the applied pressure to the AgNW film. The spring was set to 500g force at full depression of the ball into the housing. After transfer of the AgNW electrode, 300 nm Ag was thermally evaporated through a patterned shadow mask around the edges of the device leaving 1×1 cm<sup>2</sup> active area in the middle of the 1.1×1.1 cm<sup>2</sup> mesa. These bars of silver helped reduce the unnecessary series resistance in the AgNW electrode by not limiting the current collection to one geometrical direction. The nearly completed device was lights-soaked under visible illumination for 10 minutes then stored in a desiccator for 12 hours before applying the anti-reflective coating. A 111-nm-thick LiF anti-reflective coating was then added to the device. This thickness was optimized to provide anti-reflection for the visible spectrum.

## Multijunction Cell Testing Protocols

Current-voltage characteristics for the multijunction cells were measured using a Keithley model 2400 digital source meter and a Newport Oriel model # 94023A solar simulator. The solar simulator irradiance was characterized and compared to the AM1.5G spectral standard. The perovskite sub-cell's spectral mismatch factor was calculated as 0.990 using the *EQE* data from **Figure 3b**. The silicon sub-cell's spectral mismatch factor was calculated as 0.965 using the *EQE* data from **Figure 3b**. Neither the solar simulator intensity nor the calculated efficiencies were increased to account for this small spectral mismatch factor. Consequently, the reported currents and power conversion efficiencies in this manuscript are likely slightly conservative. Samples were illuminated through a 1 cm<sup>2</sup> aperture area. A 5 s delay time at each voltage step was used to try and minimize hysteresis. Longer delay times were impractical due to the limitations of the testing software. Because transient hysteretic behavior was observed for up to 30 s after setting a voltage, steady-state values of  $J_{SC}$ ,  $V_{OC}$ , and MPP were determined by setting the voltage condition for 30 s then averaging data for the next 30 s. The cell was illuminated through 1 cm<sup>2</sup> aperture mask to ensure a correct illumination area. The transient  $J_{SC}$ ,  $V_{OC}$ , and MPP curves are shown in **Figure S4**.

External quantum efficiency (*EQE*) for the tandem was recorded as a function of the wavelength using a Model SR830 DSP Lock-In Amplifier (Stanford Research Systems). A 100 W tungsten lamp (Newport) was used to provide an excitation beam, which was focused through a Princeton Instruments SpectraPro 150 monochromator. To measure the *EQE* of the perovskite sub-cell, an 870 nm infrared LED light source (Enfis) illuminated the sample to force the top perovskite sub-cell into a current-limiting regime. The monochromated signal was chopped slowly at 1.2 Hz to allow for settling of the signal. At each wavelength, the program waited for a delay time of 30 s then data was collected for 5 s. The time constant on the lock-in amplifier was 1 s. We found that the infrared chromatic bias caused an

approximately 500 mV forward bias in the silicon sub-cell, applying a 500 mV reverse bias to the perovskite sub-cell to maintain short circuit conditions. It has been shown that applying a reverse bias to many perovskite solar cells prior to and during photocurrent measurements results in a uniform decrease in the measured EQE spectrum, possibly due to a temporarily reduced current collection efficiency resulting from ion drift. To estimate the EQE spectrum of the perovskite sub-cell under broadband AM 1.5 illumination where these non-ideal operating conditions are not present, the perovskite sub-cell *EQE* was scaled by a constant factor to match the measured  $J_{sc}$ . To measure the *EQE* of the bottom Si sub-cell, a 465 nm visible LED light source (Enfis, 7mW/cm<sup>2</sup>) illuminated the sample to force the bottom Si sub-cell into a current-limiting regime. The monochromated signal was chopped quickly at 500 Hz to overcome the capacitive impedance of the perovskite sub-cell. The Si *EQE* is reported as measured.

## Steady-State Solar Simulator Measurements

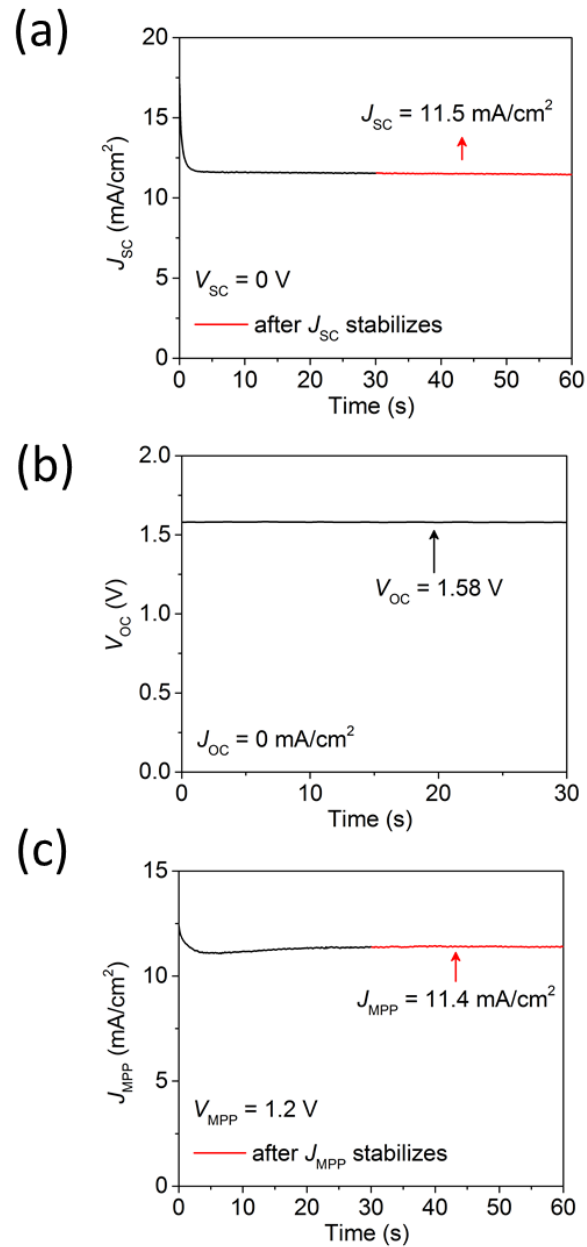


**Figure S4.** Transient (a)  $J_{SC}$ , (b)  $V_{OC}$ , and (c) MPP of the perovskite/silicon tandem cell as they stabilize over the time. The measured steady-state values are  $J_{SC} = 11.5$  mA/cm<sup>2</sup> and  $V_{OC} = 1.58$  V, respectively. The 30 s settling time for the  $V_{OC}$  is not shown as the cell was stabilized at  $V_{OC}$  for > 30 s prior to starting the measurement.

## Front/Back Illumination on Single-Junction Semi-Transparent Perovskite Cell

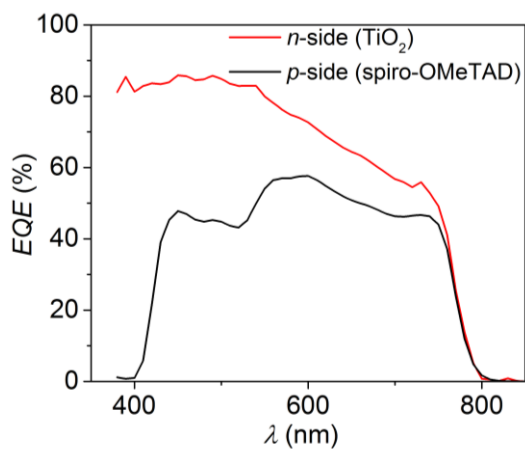


**Figure S5.** EQE of a semi-transparent perovskite solar cell illuminated through either the *n*-side (glass/TiO<sub>2</sub> side) or through the *p*-side (AgNW/spiro-OMeTAD side). The glass side EQE integrates to 17.3 mA/cm<sup>2</sup> while the AgNW side EQE integrates to 11.4 mA/cm<sup>2</sup>. This device did not have anti-reflection coatings to simplify analysis, therefore the photocurrent values are 0.5 to 1.0 mA/cm<sup>2</sup> lower than if anti-reflection coatings were used.

## Spiro-OMeTAD Optical Absorption

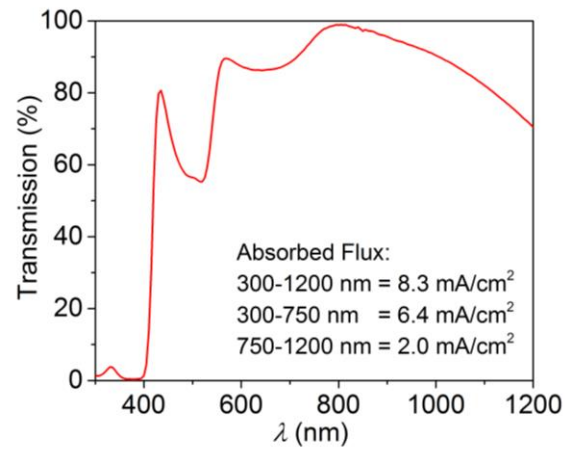


**Figure S6.** The light transmission through a 470-nm-thick doped spiro-OMeTAD film on glass measured using spectrophotometer. The contribution of the glass is removed from this plot. The absorption features from 300–400 and 450–550 nm are readily visible in the *EQE* plot above.

## Tandem Architecture Prevents Shorting of Silver Nanowire Electrode

The  $V_{oc}$  of our 2-terminal perovskite/Si multijunction has been measured as high as 1.65 V in some devices. This result is encouraging, as the  $V_{oc}$  is approximately the sum of the  $V_{oc}$  for the perovskite top sub-cell and the bottom Si sub-cell illuminated through a separate semi-transparent perovskite device on FTO (approximately 1.05 V and 0.55 V, respectively), indicating proper operation of the tunnel junction. We speculate that the tandem perovskite sub-cell's  $V_{oc}$  benefits from being in contact with silicon rather than FTO. Mechanical lamination of the AgNW electrode was previously found to be highly dependent on pressure, with too much pressure causing shorting. However, we did not observe shorting of the AgNW electrode in the tandem. This may be because the silicon emitter is not as conductive as FTO, and therefore local shorts do not affect the full device area.

## Hysteretic Behavior of the Tandem Indicates Perovskite is the Current-Limiting Sub-Cell

The slow current-dynamics and corresponding hysteresis observed in the tandem resemble the sluggish dynamics of our perovskite solar cells and suggest that the perovskite sub-cell limits the current of the tandem. To investigate further, we illuminate the tandem with a white light LED, which emits only in the visible spectrum, placing the silicon sub-cell in a current-limiting regime. In this regime, we observe the current to settle within milliseconds as expected for silicon solar cells and do not observe hysteresis. These findings are substantiated by *EQE* measurements (**Figure 3b**) of the individual sub-cells.

## References

<sup>1</sup> C.D. Bailie, M.G. Christoforo, J.P. Mailoa, A.R. Bowring, E.L. Unger, W.H. Nguyen, J. Burschka, N. Pellet, J.Z. Lee, M. Grätzel, R. Noufi, T. Buonassisi, A. Salleo, and M.D. McGehee, *Energy Environ. Sci.* (2014). DOI: 10.1039/c4ee03322a